Land Surface Temperature Estimation from the Next Generation of Geostationary Operational Environmental Satellites: GOES M–Q

DONGLIAN SUN

CEOSR, George Mason University, Fairfax, Virginia

RACHEL T. PINKER

Department of Meteorology, University of Maryland, College Park, College Park, Maryland

JEFFERY B. BASARA

Oklahoma Climatological Survey, University of Oklahoma, Norman, Oklahoma

(Manuscript received 11 October 2002, in final form 21 August 2003)

ABSTRACT

The next generation of Geostationary Operational Environmental Satellites (GOES M–Q) will have only one thermal window channel instead of the current two split-window thermal channels. There is a need to evaluate the usefulness of this new configuration to retrieve parameters that presently are derived by utilizing the split-window characteristics. Two algorithms for deriving land surface temperatures (LSTs) from the GOES M–Q series have been developed and will be presented here. Both algorithms are based on radiative transfer theory; one uses ancillary total precipitable water (TPW) data, and the other is a two-channel (3.9 and 11.0 μm) algorithm that aims to improve atmospheric correction by utilizing the middle infrared (MIR) channel. The proposed algorithms are compared with a well-known generalized split-window algorithm. It is found that by adding TPW to the 11.0-μm channel, similar results to those from the generalized split-window algorithm are attained, and the combination of 3.9 and 11.0 μm yields further improvement. GOES M–Q retrievals (simulated with *GOES-8* observations), when evaluated against skin temperature observations from the Oklahoma Mesonet, show that with the proposed two-channel algorithm, LST can be determined at an rms accuracy of about 2 K. The proposed algorithms are also applicable for the derivation of sea surface temperatures (SSTs) for which less restrictive assumptions on surface emissivity apply.

1. Introduction

Land surface temperature (LST) is an important parameter because of its control of the upward terrestrial radiation and energy exchange between the earth's surface and the atmosphere. Derivation of LST from satellite infrared radiometers has been proven to be useful. Most studies on LST have focused on the use of polar-orbiting satellite systems, such as the National Oceanic and Atmospheric Administration (NOAA) Advanced Very High Resolution Radiometer (AVHRR) (Price 1984; Becker 1987; Becker and Li 1990; Vidal and Blad 1991; Prata 1993, 1994; Sobrino et al. 1994, 1996; Coll et al. 1994; Becker and Li 1995; Coll and Caselles 1997), the along-track scanning radiometer (ATSR), and the Moderate Resolution Imaging Spectroradiometer (MODIS) (Wan and Dozier 1996; Wan and Snyder 1996; Liang 2001; Ma et al. 2002). These studies indicate that it is possible to retrieve LST at a reasonable accuracy (root-mean-square error of 1–3 K) from current operational and research satellite–borne visible/infrared radiometers. The temporal measurement frequency of the polar-orbiting satellite instruments is approximately 2 times per day, which is inadequate for many applications. The land surface temperature diurnal cycle (LSTD) is also an important element of the climate system, which cannot be captured from polar-orbiting satellites. Geostationary satellites provide diurnal coverage, which makes them attractive for deriving information on LST. Yet, less work has been done on retrieving LST from geostationary satellites. Prata and Cechet (1999) investigated LST retrieval from the Japanese *Geostationary Meteorological Satellite* (*GMS*)-*5*, using a split-window LST algorithm. LST retrieval from *GOES-8* was addressed by Faysash and Smith (1999), and by Sun and Pinker (2003). The next generation of GOES satellites will not have split-window thermal channels, and so the brightness temperature differences

Corresponding author address: Dr. Rachel T. Pinker, Department of Meteorology, Space Sciences Building, University of Maryland, College Park, College Park, MD 20742.
E-mail: pinker@atmos.umd.edu

TABLE 1. Summary of data sources.

Parameter	Institution	Instrument	Resolution	Date	Location
IGBP land cover	University of Maryland	AVHRR	1 km		Global
Surface temperature with matching atmosphere profiles	NCEP	Eta Model	2.5°	Jul 1993	Global
Satellite-viewing angles, imager data, and TPW data	University of Maryland/ NESDIS	*GOES-8*, Eta Model	0.5°	May, Oct 2001	United States
Skin temperature	Mesonet	Radiometer		May 2001	Oklahoma

of these two channels would not be available to correct for atmospheric effects. With the absence of 12.0-μm channel, alternative atmospheric correction procedures will be necessary.

In this paper, we explore the feasibility to use the total precipitable water (TPW) and the characteristics of the middle infrared (MIR) channel 3.9 μm as ancillary data to correct for atmospheric effects. The middle-infrared 3.9-μm channel has low atmospheric absorption and attenuation (May 1993; Sun and Pinker 2003); however, it contains a solar signal during the daytime, which needs to be accounted for.

The first algorithm is based on the 11.0-μm channel and the use of the total precipitable water, while the second is based on combining 11.0- and 3.9-μm channels with a solar zenith angle correction for the middle infrared 3.9-μm channel during daytime. A previously published generalized split-window algorithm (Becker and Li 1990) is chosen for comparison with the two proposed algorithms. In section 2, data used in this study are described. Section 3 presents the methodology used. Evaluation of LST estimates from simulations and from *GOES-8* data against ground observations will be presented in section 4.

2. Data used

The global reanalyzed data from National Centers for Environment Prediction (NCEP) with surface temperature and matched atmospheric profiles are used in performing simulations. Input information on surface reflectivity is based on land cover classification information. A spectral library of surface reflectivity over a wide range of spectral wavelengths (0.2–14.0 μm) from the National Aeronautics and Space Administration (NASA) Jet Propulsion Laboratory (JPL) dataset (available online at http://speclib.jpl.nasa.gov/) is used. Surface reflectivity in the GOES bands can be obtained by interpolation, based on the sensor spectral response function. The land cover data used in this study are generated at 1-km resolution at the Department of Geography, University of Maryland (Hansen et al. 2000; http:/gaia.umiacs.umd.edu:8811/landcover/index.html). This product includes 14 International Geosphere–Biosphere Programme (IGBP) classes (Turner et al. 1993), specified as follows: 1) Water; 2) evergreen needleleaf forest; 3) deciduous needleleaf forest; 4) evergreen broadleaf forest; 5) deciduous broadleaf forest; 6) mixed forest; 7) woodland; 8) wooded grassland; 9) closed shrub land; 10) open shrub land; 11) grassland; 12) cropland; 13) bare ground; 14) urban and built up. The simulations are done with inputs as available at 2.5°. The land cover product is aggregated to this resolution for the simulations, and to 0.5° for algorithm implementation. In the aggregation process, the land cover type in each grid box is assigned on the basis of the dominant surface type, while the surface emissivity is calculated according to a linear mixing, with weighted sum of the land cover percentage times the emissivity of this surface type.

Satellite observations needed for testing the methodology are available as a by-product from a NOAA/National Environmental Satellite, Data, and Information Service (NESDIS) *GOES-8* operational product on surface shortwave radiative fluxes (Tarpley et al. 1996; Pinker et al. 2003), generated in support of the Global Energy and Water Cycle Experiment (GEWEX) Continental-Scale International project (GCIP) (Leese 1994) activities, as archived at the University of Maryland (available online at http://www.atmos.umd.edu/~srb/gcip). Ground observations from the Oklahoma Mesonet are used for the evaluation of the LST algorithms. In Table 1 a summary of the data used in this study is presented.

3. Algorithm description

In the far-IR bands, the solar contributions are negligible; the outgoing infrared spectral radiance at the top of atmosphere can be presented as

$$R(\lambda, \mu) = \varepsilon_0(\lambda, \mu)B(\lambda, T_s)\tau_0(\lambda, \mu) + R_a(\lambda, \mu), \quad (1)$$

where ε_0 is the surface spectral emissivity, B is the Planck function, τ_0 is the transmittance at the earth's surface, R_a is the thermal path radiance, T_s is the skin temperature, λ is the wavelength, $\mu = \cos\theta$, and θ is the satellite-viewing angle. The satellite-viewing angle θ refers to the zenith relative to the satellite. The so-called satellite zenith angle θ_z is relative to the earth's surface. They have the following relationship:

$$\sin\theta_z = \frac{(\text{satellite height} + \text{earth radius})}{(\text{earth radius})}\sin\theta$$
$$= (36\,000 + 6700)/6700\,\sin\theta \approx 6.37\,\sin\theta. \quad (2)$$

A 2° viewing angle corresponds to 12.8° satellite zenith

angle, while a 9° viewing angle corresponds to an 85.2° satellite zenith angle.

In Eq. (1), the first term represents the surface contribution term, namely, the graybody radiance emitted by the earth's surface. The second term is the atmospheric contribution, referred to as path thermal radiance.

a. One-channel algorithm using TPW

In the atmospheric window channels, the water vapor absorption is weak. Therefore,

$$\tau_i = \exp(-k_i w \sec\theta) \approx 1 - k_i w \sec\theta, \tag{3}$$

where i denotes the channel index, k_i is the absorption coefficient at channel i, θ is the satellite-viewing angle, and w is the column water vapor. Hence,

$$d\tau_i \approx -k_i \sec\theta \, dw. \tag{4}$$

The measured radiance in the thermal window region can be expressed from the radiative transfer equation (RTE) with respect to the channel value as

$$R_i = \varepsilon_i B_i(T_s)\tau_i + \int_0^{\tau} B_i(T_p)\, d\tau \approx \varepsilon_i B_i(T_s)(1 - k_i W \sec\theta) + k_i \sec\theta \int_0^{w} B_i(T_p)\, dw, \tag{5}$$

where B_i is the Planck function weighted for channel i, T_i is the brightness temperature (K), measured at the satellite level in channel i, T_s is the surface skin temperature (K), ε_i and τ_i are the surface emissivity and atmospheric transmittance in channel i, T_p is the air temperature (K) at vertical layer p, p is the pressure of the vertical emitting layer (hPa), and W represents the TPW (cm). Equation (5) is a simplification of Eq. (1), considering channel values instead of spectral values. We define an atmospheric mean Planck radiance

$$B_i(T_a) = \frac{\int_0^{w} B(T_p)\, dw}{\int_0^{w} dw}, \tag{6}$$

where T_a is the atmospheric mean temperature. Inserting Eq. (6) into Eq. (5) will yield

$$R_i \approx \varepsilon_i B_i(T_s)(1 - k_i W \sec\theta) + k_i \sec\theta W B_i(T_a). \tag{7}$$

The Planck function can be expanded into a Taylor series about the brightness temperature T_i in the form of

$$R_i = B_i(T_i) = \frac{DB}{DT}\bigg|_{T_i} \frac{B(T_{ii})}{\dfrac{DB}{DT}\bigg|_{T_i}} = \frac{DB}{DT}\bigg|_{T_i} L(T_i),$$

$$B_i(T_s) \approx B_i(T_i) + \frac{DB}{DT}\bigg|_{T_i} (T_s - T_i) = \frac{DB}{DT}\bigg|_{T_i} [T_s - T_i + L(T_i)], \quad \text{and}$$

$$B_i(T_a) \approx B_i(T_i) + \frac{DB}{DT}\bigg|_{T_i} (T_a - T_i) = \frac{DB}{DT}\bigg|_{T_i} [T_a - T_i + L(T_i)]. \tag{8}$$

Inserting Eq. (8) into Eq. (7) will linearize the RTE with respect to temperature:

$$L(T_i) \approx \varepsilon_i(1 - k_i w \sec\theta)[T_s - T_i + L(T_i)] + k_i w \sec\theta [T_a - T_i + L(T_i)]. \tag{9}$$

Several approximations have been proposed for $L(T_i)$. Sun and Pinker (2003) use

$$L(T_i) \approx T_i/n_i. \tag{10}$$

By inserting Eq. (10) into Eq. (9),

$$(C_{i1}T_i - \varepsilon_i T_s) = (T_a - \varepsilon_i T_s - C_{i2}T_i)k_i W \sec\theta, \tag{11}$$

where

$$C_{i1} = \frac{1 + (n_i - 1)\varepsilon_i}{n_i} \quad \text{and}$$

$$C_{i2} = \frac{(n_i - 1)(1 - \varepsilon_i)}{n_i}. \tag{11a}$$

Let i represent the 11.0-μm channel. For most land surfaces and for the ocean, the emissivity at 11.0 μm is essentially unity.

In order to reduce the number of unknown variables, we assume that the atmospheric mean temperature T_a is proportional to the surface temperature T_s,

$$T_a \approx a_w T_s. \tag{12}$$

This assumption may introduce errors if the surface emissivity at the 11.0-μm channel is not close to unity.

A solution for T_s can be obtained as follows:

$$T_s \approx \frac{T_i}{[(a_w - 1)k_i W \sec\theta + 1]} = \frac{T_{11}}{cW \sec\theta + 1}. \tag{13}$$

If this equation is adopted to every land surface, then

$$T_s(k) \approx \frac{T_{11}}{C(k)W \sec\theta + 1} \approx c_1(k) + c_2(k)T_{11} + c_3(k)W \sec\theta, \tag{14}$$

where k is the surface-type index. In order to evaluate the proposed algorithm with *GOES-8* observations, simulations are performed for the spectral response function of the *GOES-8* imager; sensor noise and calibration errors are not included. Table 2 presents coefficients for Eq. (14).

TABLE 2. Coefficients for the one-channel algorithm in Eq. (14).

Surface-type index	c_0	c_1	c_2
1	−2.0566	1.0128	1.3042
2	86.1229	0.6919	2.1848
3	−13.4161	1.0595	0.7137
5	278.5000	-5.7916×10^{-11}	-1.4305×10^{-8}
6	115.9919	0.5591	7.3821
7	0.1735	1.0073	1.2601
8	−21.1318	1.1103	−0.4244
9	46.2754	0.8481	1.5118
10	2.4896	1.0076	0.8698
11	−14.3104	1.0668	0.3947
12	−12.9910	1.0561	0.8115
13	0.6159	1.0076	1.1648

b. The 3.9- and 11.0-μm two-channel algorithm

The path thermal radiance in Eq. (1) represents the vertically integrated effect of emission from every atmospheric layer, modulated by the transmittance of the above layer. In spectral form, it can be represented as

$$R_a(\lambda, \mu) = \int_{\tau_0}^{1} B(\lambda, T_p)\, d\tau(\lambda, \mu, p), \qquad (15)$$

where B, λ, and μ are as given in Eq. (1), and T_p and p are as given in Eq. (5). Therefore, for the thermal infrared 11.0-μm channel, the outgoing infrared spectral radiance at the top of atmosphere can be represented in spectral form as

$$R(\lambda, \mu) = \varepsilon_0(\lambda, \mu)B(\lambda, T_s)\tau_0(\lambda, \mu) + \int_{\tau_0}^{1} B(\lambda, T_p)\, d\tau(\lambda, \mu, p), \qquad (16)$$

where ε_0, B, T_s, τ_0, λ, and μ are the same as in Eq. (1); T_p and p are as given in Eq. (5).

During nighttime, the MIR radiance for the 3.9-μm channel is represented by Eq. (16). During daytime, the solar radiation reflected by the earth's surface needs to be accounted for, and, therefore, the outgoing infrared spectral radiance at the top of atmosphere is represented as

$$R(\lambda, \mu) = \varepsilon_0(\lambda, \mu)B(\lambda, T_s)\tau_0(\lambda, \mu) + \int_{\tau_0}^{1} B(\lambda, T_p)\, d\tau(\lambda, \mu, p) + \frac{E_{\text{solar}}}{d} \cos\theta_s \rho_b(\theta_s, \theta)\tau_0(\lambda, \mu), \qquad (17)$$

where E_{solar} is the solar constant, d is the earth–sun distance, θ_s is solar zenith angle, and ρ_b is the bidirectional reflectivity of the surface. During nighttime, the outgoing infrared spectral radiance at the top of atmosphere in the 11.0- and 3.9-μm channels can be represented by Eq. (16). Based on Eq. (16), for a specific land surface type, with surface emissivity close to unity, the radiance error introduced by the atmosphere, ΔR, can be represented as

$$\begin{aligned}\Delta R &= B(\lambda, T_s) - R(\lambda, \mu)\\ &= B(\lambda, T_s) - B(\lambda, T_s)\tau_0(\lambda, \mu) - \int_{\tau_0}^{1} B(\lambda, T_p)\, d\tau(\lambda, \mu, p)\\ &= \int_{\tau_0}^{1} B(\lambda, T_s)\, d\tau(\lambda, \mu, p) - \int_{\tau_0}^{1} B(\lambda, T_p)\, d\tau(\lambda, \mu, p)\\ &= \int_{\tau_0}^{1} [B(\lambda, T_s) - B(\lambda, T_p)]\, d\tau(\lambda, \mu, p). \qquad (18)\end{aligned}$$

In the atmospheric window regions, the absorption is weak, so that

$$\tau = e^{-k_\lambda u} \approx 1 - k_\lambda u, \qquad (19)$$

where k_λ is the absorption coefficients at wavelength λ and u is absorption gas optical path (mainly water vapor in window channel). Under this assumption, Eq. (18) can be written as

$$\begin{aligned}\Delta R &\approx k_\lambda \int_0^{u_s} [B(\lambda, T_s) - B(\lambda, T_p)]\, du\\ &\approx \left.\frac{\partial B}{\partial T}\right|_{T_s} k_\lambda \int_0^{u_s} (T_s - T_p)\, du, \qquad (20)\end{aligned}$$

where u_s is the total optical depth from the surface to the top of atmosphere. From the Planck function we get

$$\Delta R = B(\lambda, T_s) - R(\lambda, \mu) = B(\lambda, T_s) - B(\lambda, T_\lambda) \approx \left.\frac{\partial B}{\partial T}\right|_{T_s} (T_s - T_\lambda), \qquad (21)$$

where T_λ is brightness temperature at wavelength λ.

From Eqs. (20) and (21), it follows that

$$T_s - T_\lambda = k_\lambda \int_0^{u_s} (T_s - T_p)\, dl. \qquad (22)$$

Using the 11.0- and 3.9-μm channels (nighttime), two equations with different absorption coefficient k_λ can be solved simultaneously to yield

$$T_s - T_{11} = \left(\frac{k_{11}}{k_{3.9} - k_{11}}\right)(T_{11} - T_{3.9}). \qquad (23)$$

Equation (23) is derived based on the assumption that surface emissivity is close to unity, and, therefore, it can be applied to any surface type (land or water), as long as this assumption is valid. However, for some land

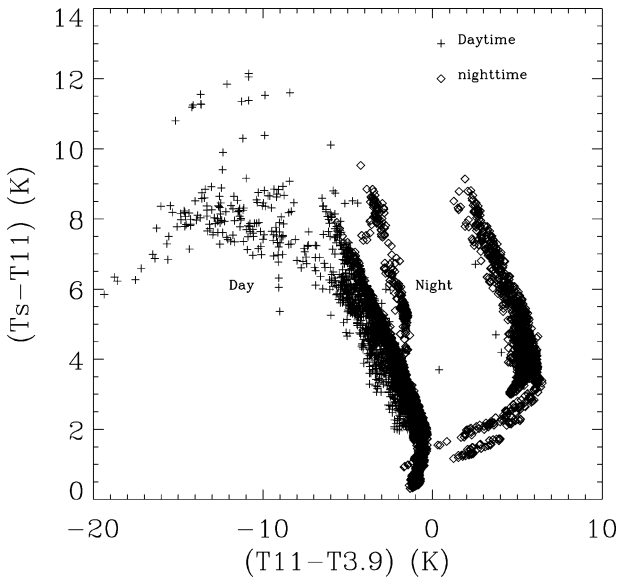

FIG. 1. Distribution ($T_s - T_{11}$) vs ($T_{11} - T_{3.9}$), obtained from the simulations with MODTRAN using the NCEP global reanalyzed data for Jul 1993; T_{11} and $T_{3.9}$ are the simulated *GOES-8* brightness temperatures in channels 4 and 2, and T_s is the skin temperature from the NCEP data used as input for forward simulations.

surface types, the surface emissivities are not close to unity, particularly in the 3.9-μm channel. Therefore, the actual relationship between the temperature deficits ($T_s - T_{11}$) and ($T_{11} - T_{3.9}$) may not be as linear as derived from the radiative transfer equations. From Fig. 1 derived from the Moderate-Resolution Atmospheric Radiance and Transmittance Model (MODTRAN) simulations using the NCEP global reanalyzed data for July of 1993, it is evident that a reverse parabolic relationship exists between ($T_s - T_{11}$) and ($T_{11} - T_{3.9}$). If the satellite-viewing correction term ($\sec\theta - 1$) proposed by McClain et al. (1985) is added to the nighttime LST retrieval equation, we get

$$T_s(k) = a_0(k) + a_1(k)T_{11} + a_2(k)(T_{11} - T_{3.9}) + a_3(k)(T_{11} - T_{3.9})^2 + a_4(k)(\sec\theta - 1), \quad (24)$$

where k is the surface type index, $k = 1$–14.

As is also evident from Fig. 1, during daytime, the brightness temperature deficits ($T_{11} - T_{3.9}$) have large negative values because the brightness temperature in the middle infrared channel contains the solar radiation reflected by the earth surface. To reduce the solar signal contamination in the brightness temperature, the solar contribution should be subtracted from the observed middle infrared signal:

$$T_{3.9} = T_{3.9} - f^{-1}\left[\frac{E_{\text{solar}}}{d}\cos\theta_s\rho_b(\theta_s, \theta)\tau_0(\lambda, \mu)\right], \quad (25)$$

where E_{solar} is the solar constant and d is the sun–earth distance. For a specific surface type, the bidirectional effect depends on the solar zenith angle θ_s and the satellite-viewing angle θ. From Eq. (19), the surface transmittance τ_0 can be approximated as

$$\tau_0(\lambda, \mu) \approx 1 - k_\lambda u_s, \quad (25a)$$

where u_s is the atmospheric total optical path, given as

$$u_s = \int_0^\infty \rho\, ds = \int_0^\infty \rho \sec\theta\, dz, \quad (25b)$$

where ρ is density of the atmospheric absorption gas, s is the geometry path, and z is the height. Therefore, the solar correction term in Eq. (25) is a function of atmospheric total optical path u_s, satellite zenith angle θ, and solar zenith angle θ_s, given as

$$T'_{3.9} = T_{3.9} - f^{-1}\left[\frac{E_{\text{solar}}}{d}\cos\theta_s\rho_b(\theta_s, \theta)\tau_0(\lambda, \mu)\right] \approx T_{3.9} - [c_0(k) + c_1(k)u_s\cos\theta_s]. \quad (25c)$$

The coefficients in (25c) depend on surface type. In the window channels, the major absorbing gas is the water vapor; neglecting absorption from CH_4 and N_2O in the 3.9-μm channel can contribute to additional errors. Estimation of atmospheric CH_4 and N_2O amounts is difficult. To allow for the effect of all absorbers in this channel, we propose to use the brightness temperature $T_{3.9}$ to replace u_s in (25c), by modifying the coefficients in this equation as follows:

$$T'_{3.9} \approx T_{3.9} - [c'_0(k) + c'_1(k)T_{3.9}\cos\theta_s]. \quad (25d)$$

During daytime, $T_{3.9}$ in Eq. (24) should be replaced by $T'_{3.9}$. Ignoring the second term of $\cos\theta_s$ in Eq. (24), we have

$$T_s(k) = a_0(k) + a_1(k)T_{11} + a_2(k)(T_{11} - T_{3.9}) + a_3(k)(T_{11} - T_{3.9})^2 + a_4(k)(\sec\theta - 1) + a_5(k)T_{3.9}\cos\theta_s, \quad (26)$$

where k is the surface type index.

The algorithms proposed here, as formulated by Eqs. (14), (24), and (26), use surface types instead of the traditional surface emissivity information. It is expected that this will reduce the surface temperature retrieval error due to lack of information on surface emissivity. The coefficients are obtained from the forward simulations and are presented in Table 3 for nighttime and in Table 4 for daytime.

Comparison was made with results obtained from the generalized split-window algorithm (Becker and Li 1990; Wan and Dozier 1996), given as

$$T_s = A_0 + P\frac{T_{11} + T_{12}}{2} + M\frac{T_{11} - T_{12}}{2}, \quad (27)$$

where T is the brightness temperature; subscripts 11 and 12 represent 11.0- and 12.0-μm bands, respectively.

In order to make the comparison realistic, the coefficients for the generalized split-window algorithm are also derived from the *GOES-8* simulations:

TABLE 3. Coefficients for the two-channel nighttime algorithm in Eq. (24).

Surface-type index	a_0	a_1	a_2	a_3	a_4
1	−11.7492	1.0495	−0.3869	0.1122	205.9218
2	−8.3492	1.0385	1.0068	1.1253	288.3721
3	−23.4898	1.1030	2.4371	0.7713	223.5892
5	278.4974	0.0001	0.0001	0.0000	0.0002
6	−68.4020	1.2598	−6.0778	−5.0418	82.4269
7	−21.5562	1.0902	1.6008	0.7690	245.7784
8	−30.1544	1.1074	−3.8824	−0.4056	278.6821
9	−29.0388	1.1154	−1.7161	−0.1940	280.6394
10	−16.0033	1.0849	3.8626	1.4256	239.8922
11	−20.1564	1.0970	3.2339	0.8758	224.5892
12	−12.9611	1.0530	−0.1669	0.3429	265.0296
13	−17.6040	1.0962	−1.3910	0.0814	195.2467

$$A_0 = -13.2734,$$

$$P = 1.0635 + 0.1111\frac{1-\varepsilon}{\varepsilon} - 0.1829\frac{\Delta\varepsilon}{\varepsilon^2}, \quad \text{and}$$

$$M = 4.6930 - 18.1606\frac{1-\varepsilon}{\varepsilon} + 23.7890\frac{\Delta\varepsilon}{\varepsilon^2}, \quad (27a)$$

where $\varepsilon = (\varepsilon_{11} + \varepsilon_{12})/2$, and $\Delta\varepsilon = \varepsilon_{11} - \varepsilon_{12}$. Emissivity information needed for the generalized split-window algorithm is assigned according to surface types as proposed by Snyder et al. (1998).

4. Results

a. Simulations

To make the LST simulation results applicable on a global scale, the forward simulations are performed with MODTRAN (Berk et al. 1989), using the NCEP global reanalyzed data for July 1993 as input. Using the proposed GOES M–Q algorithms, as well as the Becker and Li (1990) generalized split-window algorithm, the simulated *GOES-8* LST rms, bias, and standard deviations are derived and shown in Figs. 2, 3, and 4. The results from the proposed one-channel algorithm are comparable to those from the generalized split-window algorithm. The results from the two-channel algorithm show improvements when compared with the generalized split-window algorithm. For all the algorithms, the LST retrieval error increases with satellite-viewing angle; largest error occurs at temperature above 280 K. The maximum rms and bias errors are 4 and −4 K, respectively, for the generalized split-window algorithm, 2.5 and −1.5 K for the one-channel algorithm, and 1.5 and −1.0 K for the two-channel algorithm. The maximum standard deviation is 1.25 K for both the generalized split-window and the one-channel algorithm, and 0.75 K for the two-channel algorithm. In the above analysis, the TPW used in the one-channel algorithm was integrated from the atmospheric profiles of the NCEP reanalyzed data. Based on Figs. 2 and 3, the two-channel algorithm is the best, followed by the one-channel and split-window algorithms. For temperatures above 300 K and satellite-viewing angles greater than 6°, the two-channel algorithm performs best, followed by the split-window and one-channel algorithms (Fig. 4). For temperatures below 290 K, the proposed algorithms are less accurate than the generalized split-window algorithm.

During daytime, the LST retrieval errors from the proposed two-channel algorithm, with and without solar correction, are compared with those from the generalized split-window algorithm. The two-channel algo-

TABLE 4. Coefficients for the two-channel daytime algorithm in Eq. (26).

Surface-type index	a_0	a_1	a_2	a_3	a_4	a_5
1	−19.9562	1.0705	−1.4295	−0.0069	276.7415	−0.0088
2	−22.3184	1.0284	−10.2682	−1.2986	89.8689	0.0223
3	−18.5569	1.0781	0.0361	0.1129	287.6658	−0.0096
5	278.4544	0.6632	−1.1929	-8.8×10^{-5}	4.238×10^{-3}	−0.6630
6	−68.4020	2.6401	−7.4581	−5.0418	82.4269	−1.3803
7	−23.6544	1.0899	−0.9280	0.0411	295.0065	−0.0152
8	−65.5309	1.2663	0.2151	0.0452	392.5620	−0.0421
9	10.4302	1.0066	0.7868	0.0836	365.8796	−0.0302
10	−23.4334	1.0943	−1.6155	0.0084	274.2646	−0.0675
11	−10.6280	1.0676	1.4115	0.2408	325.4508	−0.0186
12	−35.3674	1.1236	−2.1606	−0.0272	253.9508	−0.0288
13	−75.2268	1.2895	−0.7542	−0.0036	463.5401	−0.0694

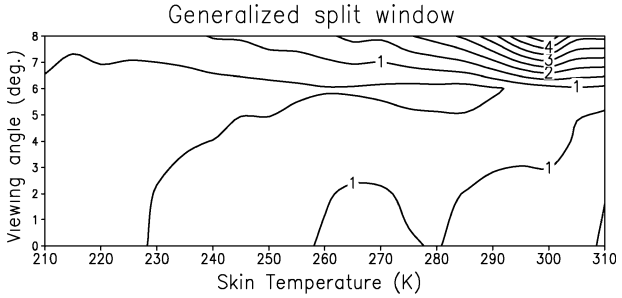

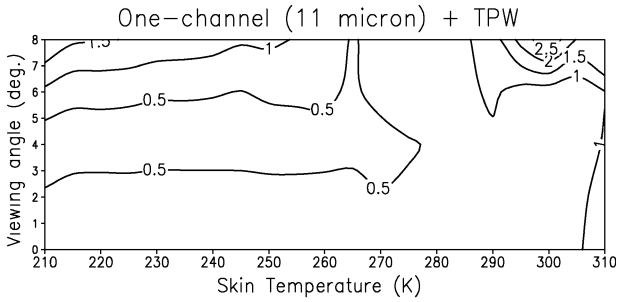

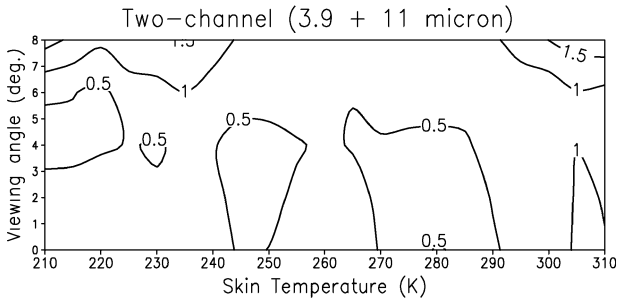

FIG. 2. Rms errors in surface skin temperature vs satellite-viewing angle from *GOES-8* simulations of proposed GOES M–Q algorithms are compared with the generalized split-window algorithm.

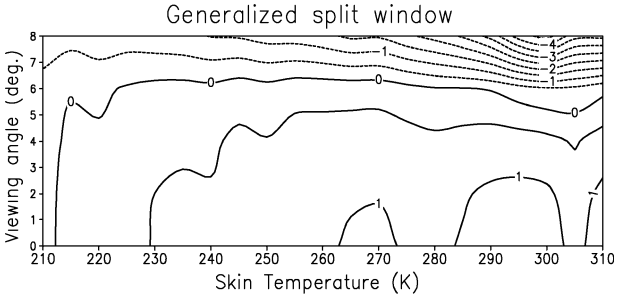

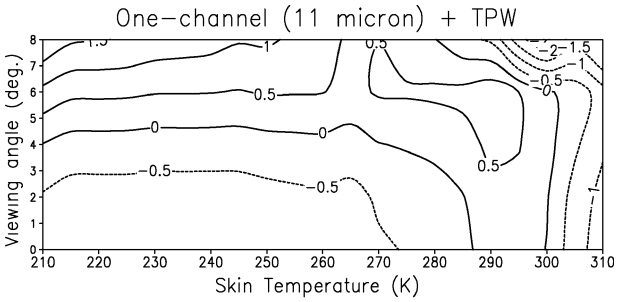

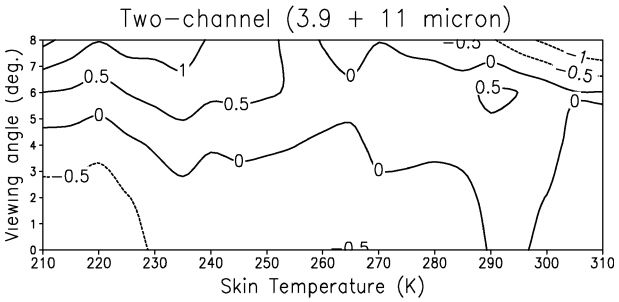

FIG. 3. Bias errors in surface skin temperature vs satellite-viewing angle from GOES M–Q simulations and the generalized split-window algorithm.

rithm with solar zenith correction shows improvement over that without solar correction (Fig. 5).

b. Evaluation

Skin temperatures as observed with infrared thermometers (IRT) at the Oklahoma Mesonet network of 115 sites are used to evaluate the LST algorithms proposed for GOES M–Q. The Oklahoma Mesonet began in 1991 as a statewide mesoscale environmental and hydrometeorological monitoring network (Brock et al. 1995; Fiebrich et al. 2003). The integrated surface types at the Mesonet sites are predominantly grassland/wooded grassland/cropland. The range of emissivities for these surface types is 0.88–0.95 for the 3.9-μm channel, and 0.95–0.98 for the 11.0-μm channel. The *GOES-8* target mean brightness temperature and the TPW data from the Eta model are used to retrieve LST. Time series of the retrieved skin temperature at two Mesonet sites using the proposed algorithms and the generalized split-window algorithm are shown in Fig. 6. All algorithms capture the strong diurnal cycle in the skin temperature with a random noise on the order of 1–2 K. Results from the generalized split-window algorithm are in closest agreement with the observed temperatures. The proposed one- and two- channel algorithms produce positive and negative bias errors, respectively. Histograms of the temperature retrieval errors (retrieval minus observations) for different algorithms are given in Fig. 7. A total of 3348 clear samples are selected (when cloud fraction was less than 5%). For the generalized split-window algorithm, the average retrieval rms error is 1.8 K; the bias error is -0.9 K, with a standard deviation of 1.6 K. For the one-channel algorithm, the average retrieval rms error is 2.3 K; the bias error is 0.5 K, with a standard deviation of 2.2 K. For the two-channel algorithm, the average rms error is 2.7 K; the bias error is -2.2 K, with a standard deviation of 1.4 K. The skin temperature retrieval errors are in the range from -0.5 to 0.5 K for the generalized split-window algorithm, from 0 to 2.0 K for the one-channel algorithm, and from -1.5 to -0.5 K for the two-channel algorithm. The

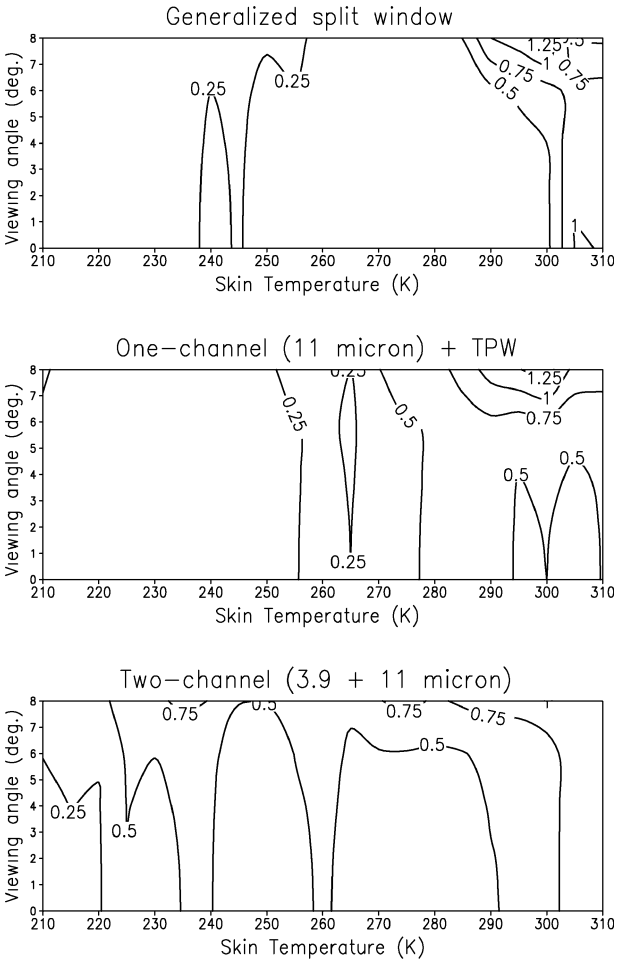

FIG. 4. Standard deviation error in surface skin temperature vs satellite-viewing angle from *GOES-8* simulations of proposed GOES M–Q algorithms are compared with the generalized split-window algorithm.

evaluations indicate that the generalized split-window algorithm performs better than the proposed algorithms for the next generation of GOES M–Q. In the above evaluations, coefficients derived independently from the forward simulations with the NCEP global reanalyzed data were used.

An experiment is performed using coefficients trained from about half randomly selected samples of actual observations in the Mesonet area. The results are as follows: for the generalized split-window algorithm, the average rms is 2.1 K, the bias is 0.2 K, and the standard deviation is 2.0 K. For the one-channel algorithm, the average rms is 3.1 K, the bias is −0.5 K, and the standard deviation is 3.0 K. For the two-channel algorithm, the average rms is 2.2 K, the bias is 0.3 K, and the standard deviation is 2.1 K. The two-channel algorithm is comparable to the generalized split-window algorithm, while the one-channel algorithm is the least accurate. When compared with simulation results, the outcome from this experiment is more consistent than the one obtained from the previous evaluation.

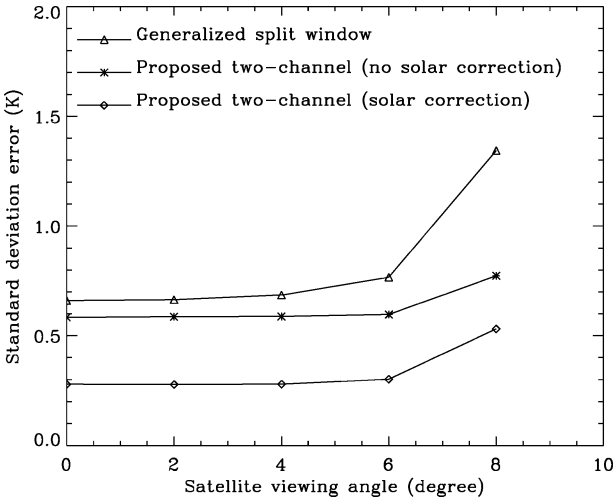

FIG. 5. Standard deviation from simulations vs satellite-viewing angle for different algorithms during daytime.

5. Algorithm error analysis

Differences between simulations and observations can be due to the following:

1) Algorithm coefficients, derived from global simulations, may not be optimized for the Mesonet area.
2) Sensor noise and calibration errors are not included

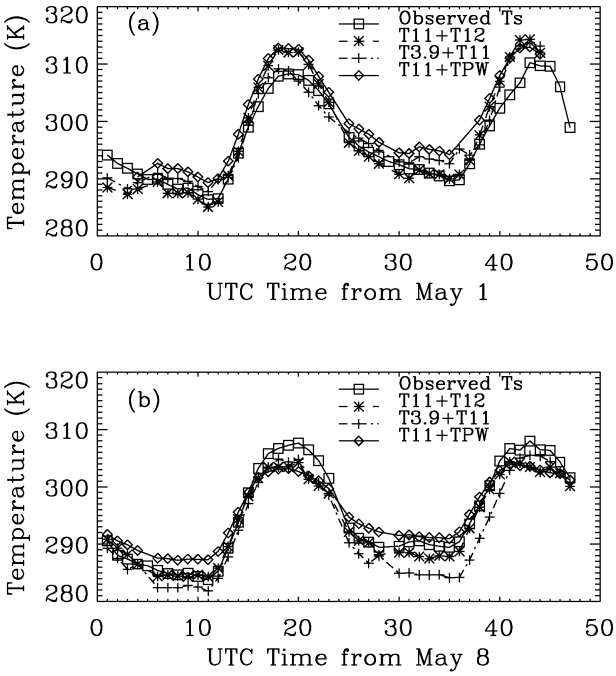

FIG. 6. Time series of retrieved and observed temperatures in Oklahoma at (a) Arnett (36.07°N, 99.90°W), 1–2 May 2001, and (b) Byars (34.85°N, 97.00°W), 8–9 May 2001.

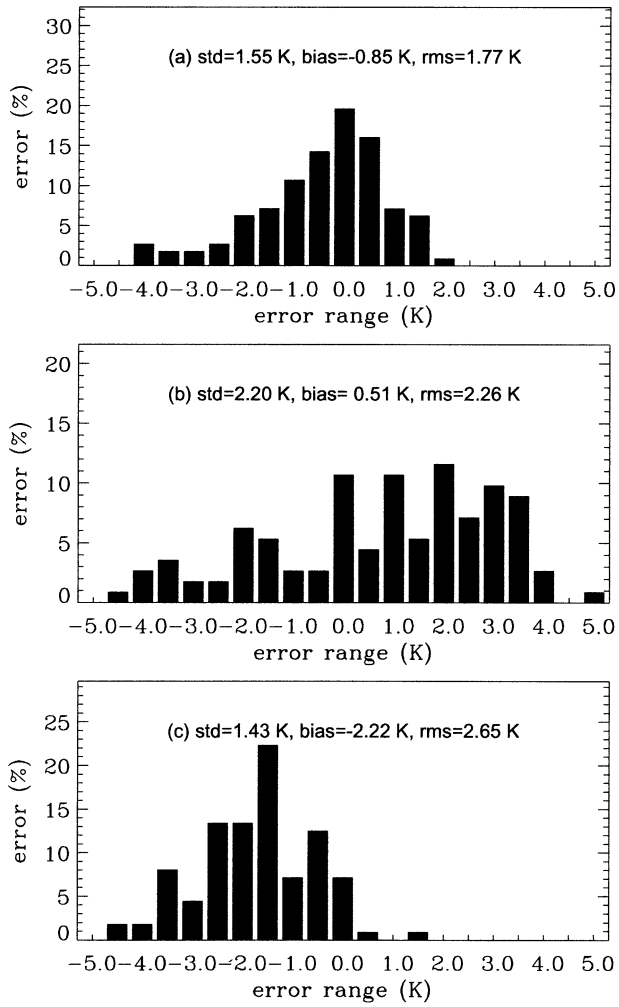

FIG. 7. Histograms of skin temperature retrieval errors (retrieval minus observation) at Mesonet sites during 1–31 May 2001.

in the forward simulations, but are included in *GOES-8* observations. The noise equivalent difference temperature (NEDT) is about 0.1–0.2 K at 300 K (see online at http://rsd.gsfc.nasa.gov/goes/text/goestechnotes.html).

3) The proposed solar correction scheme is simplistic; the Mesonet sites are viewed in the backscattering direction of the *GOES-8* and not all bidirectional effects are accounted for (the bidirectional effects in the middle infrared channels were considered in the simulations).
4) In the derivation of the one-channel algorithm, the assumption that the mean atmospheric temperature T_a is proportional to the skin temperature T_s may introduce errors, if the surface emissivity at the 11.0-μm channel is not close to unity. The Mesonet sites are predominantly grassland/wooded and grassland/cropland for which the range of the surface emissivity is 0.95–0.98 at the 11.0-μm channel.
5) In May, the temperature range for the Mesonet area is 275–310 K, when the water vapor amount is the highest, resulting in larger LST retrieval errors than on the average (Sun and Pinker 2003).
6) In the formulation of the one-channel algorithm, it was assumed that the atmospheric absorption in the 11.0-μm channel is mainly due to water vapor, ignoring the contribution of other absorbing gases. Kratz and Rose (1999) found that for midlatitude summer atmosphere, neglecting contributions from molecular species in the correlated *k* distribution (except H_2O and O_3) overestimates the upwelling top of atmosphere (TOA) flux within the 8.0–12.0-μm range by 1.5%.
7) The TPW data used in the evaluation are from the Eta Model output and may not be accurate.
8) The assumed clear pixels could be cloud contaminated. Heidinger et al. (2002) used MODIS data to study cloud contamination in the AVHRR data, and found that the contamination of the clear pixels in the 1-km AVHRR data was between 1% and 3%. The levels of contamination of the 4-km pixels ranged from 2% to 4%. We performed an experiment using 1/8° resolution data to study cloud contamination within a 1/2° grid. It was found that the use of the 1/8° resolution data could improve rms error by about 0.2–0.3 K when compared with the 1/2° resolution errors.
9) The satellite observations and the ground observations are at different spatial scales, with *GOES-8* having a 4-km resolution, while the ground observations are local.
10) The accuracy of the IRT used by the Oklahoma Mesonet for skin temperature measurement is approximately ±0.2 K from 288 to 305 K and ±0.3 K from 278 to 318 K (Bugbee et al. 1998).

6. Conclusions and discussion

In the absence of the 12.0-μm channel in the next generation of the GOES M–Q imager, the conventional split-window LST retrieval methodology would not be applicable. In this study, alternative options to derive surface temperature using total precipitable water information or a combination of 3.9- and 11.0-μm channels during both daytime and nighttime are evaluated. A strategy for correcting solar contamination of the middle infrared radiances is also explored. Simulation results indicate that the alternative options are comparable to the split-window approach. Evaluation of LST retrievals from *GOES-8* data against the Oklahoma Mesonet observations during May 2001 shows that for the one-channel algorithm, the rms error is 2.2 K and the bias error is 0.5 K; for the two-channel algorithm, the rms error is 2.6 K and the bias error is 2.2 K; and for the generalized split-window algorithm, the rms error is 1.8 K and the bias error is −0.9 K. The larger errors from the actual *GOES-8* observations as compared with

the simulations are partially correlated with the noise and the calibration errors in the satellite radiances. Additional possible sources of errors are the TPW data and the ground observations used for evaluations.

Acknowledgments. The authors thank Wen Meng and Qian-Hong Li for their help in processing the clear-sky radiances in the GCIP/SRB product for use in this study, under support from Grants NA86GP0202, NAG59916, and NA06GP0404 from the NOAA Office of Global Programs.

REFERENCES

Becker, F., 1987: The impact of spectral emissivity on the measurement of land surface temperature from a satellite. *Int. J. Remote Sens.,* **11,** 369–394.

——, and Z. L. Li, 1990: Toward a local split window method over land surface. *Int. J. Remote Sens.,* **11,** 369–393.

——, and ——, 1995: Surface temperature and emissivity at various scales: Definition, measurement and related problems. *Remote Sens. Rev.,* **12,** 225–253.

Berk, A., L. S. Bernstein, and D. C. Robertson, 1989: MODTRAN, A moderate resolution model for LOWTRAN. Spectral Sciences, Inc. Rep. GL-TR-89-0122, 48 pp.

Brock, F. V., K. C. Crawford, R. L. Elliott, G. W. Cuperus, S. J. Stadler, H. L. Johnson, and M. D. Eilts, 1995: The Oklahoma Mesonet: A technical overview. *J. Atmos. Oceanic Technol.,* **12,** 5–19.

Bugbee, B., M. Droter, O. Monje, and B. Tanner, 1998: Evaluation and modification of commercial infrared transducers for leaf temperature measurement. *Adv. Space Res.,* **22,** 1425–1434.

Coll, C., and V. Caselles, 1997: A split-window algorithm for land surfaces temperature from Advanced Very High-Resolution Radiometer data: Validation and algorithm comparison. *J. Geophys. Res.,* **102,** 16 697–16 713.

——, ——, J. A. Sobrino, and E. Valor, 1994: On the atmospheric dependence of the split-window equation for land surface temperature. *Int. J. Remote Sens.,* **15,** 105–122.

Faysash, D. A., and E. A. Smith, 1999: Simultaneous land surface temperature–emissivity retrieved in the infrared split window. *J. Atmos. Oceanic Technol.,* **16,** 1673–1689.

Fiebrich, C. A., J. E. Martinez, J. A. Brotzge, and J. B. Basara, 2003: The Oklahoma Mesonet's skin temperature network. *J. Atmos. Oceanic Technol.,* **20,** 1496–1504.

Hansen, M. C., R. S. Defries, J. R. G. Townshend, and R. Sohlberg, 2000: Global land cover classification at 1 km resolution using a classification tree approach. *Int. J. Remote Sens.,* **21,** 1331–1364.

Heidinger, A. K., V. R. Anne, and C. Dean, 2002: Using MODIS to estimate cloud contamination of the AVHRR data record. *J. Atmos. Oceanic Technol.,* **19,** 586–601.

Kratz, D. P., and F. G. Rose, 1999: Accounting for molecular absorption within the spectral range of the CERES window channel. *J. Quant. Spectrosc. Radiat. Transfer,* **61,** 83–95.

Leese, J. A., 1994: *Implementation Plan for the GEWEX Continental Scale International Project (GCIP).* Vol. 3, *Strategy Plan for Data Management,* International GEWEX Project Office Publication Series, 49 pp.

Liang, S., 2001: An optimization algorithm for separating land surface temperature and emissivity from multispectral thermal infrared imagery. *IEEE Trans. Geosci. Remote Sens.,* **39,** 264–274.

Ma, X. L., Z. Wan, C. C. Moeller, W. P. Menzel, and L. E. Gumley, 2002: Simultaneous retrieval of atmospheric profiles, land surface temperature, and surface emissivity from moderate resolution imaging spectroradiometer thermal infrared data: Extension of a two-step physical algorithm. *Appl. Opt.,* **41,** 909–924.

May, D. A., 1993: Global and regional comparative performance of linear and non-linear satellite multichannel sea surface temperature algorithms. Naval Research Laboratory Tech. Rep. NRL/MR/7240-93-7049, 36 pp.

McClain, E. P., W. G. Pichel, and C. C. Walton, 1985: Comparative performance of AVHRR-based multichannel sea surface temperatures. *J. Geophys. Res.,* **90,** 11 587–11 601.

Pinker, R. T., and Coauthors, 2003: Surface radiation budgets in support of the GEWEX Continental Scale International Project (GCIP) and the GEWEX Americas Prediction Project (GAPP), including the North American Land Data Assimilation System (NLDAS) project. *J. Geophys. Res.,* **108,** 8844, doi:10.1029/2002JD003301.

Prata, A. J., 1993: Land surface temperatures derived from the Advanced Very High Resolution Radiometer and the Along-Track Scanning Radiometer. I. Theory. *J. Geophys. Res.,* **98,** 16 689–16 702.

——, 1994: Land surface temperatures derived from the Advanced Very High Resolution Radiometer and the Along-Track Scanning Radiometer. 2. Experimental results and validation of AVHRR algorithms. *J. Geophys. Res.,* **99** (D6), 13 025–13 058.

——, and R. P. Cechet, 1999: An assessment of the accuracy of land surface temperature determination from the *GMS-5* VISSR. *Remote Sens. Environ.,* **67,** 1–14.

Price, J. C., 1984: Land surface temperature measurements from the split window channels of the *NOAA-7*/AVHRR. *J. Geophys. Res.,* **89,** 7231–7237.

Snyder, W., Z. Wan, Y. Zhang, and Y. Feng, 1998: Classification-based emissivity for land surface temperature measurement from space. *Int. J. Remote Sens.,* **19,** 2753–2772.

Sobrino, J. A., Z. L. Li, M. P. Stoll, and F. Becker, 1994: Improvements in the split window technique for land surface temperature determination. *IEEE Trans. Geosci. Remote Sens.,* **32,** 243–253.

——, ——, ——, and ——, 1996: Multi-channel and multi-angle algorithms for estimating sea and land surface temperature with ATSR data. *Int. J. Remote Sens.,* **17,** 2089–2114.

Sun, D., and R. T. Pinker, 2003: Estimation of land surface temperature from a Geostationary Operational Environmental Satellite (*GOES-8*). *J. Geophys. Res.,* **108**, 4326, doi:10.1029/2002JD002422.

Tarpley, J. D., R. T. Pinker, and I. Laszlo, 1996: Experimental GOES shortwave radiation budget for GCIP. *Proc. Second Int. Scientific Conf. on the Global Energy and Water Cycle,* Washington, DC, WCRP, 284–285.

Turner, B. L., R. H. Moss, and D. L. Skole, 1993: Relating land use and global land-cover change: A proposal for an IGBP-HDP core project. Swedish Academy of Sciences IGBP Rep. 24, 65 pp.

Vidal, R. C., and B. L. Blad, 1991: Atmospheric and emissivity correction of land surface temperature measured from satellite using ground measurements or satellite data. *Int. J. Remote Sens.,* **12,** 2449–2460.

Wan, Z., and J. Dozier, 1996: A generalized split-window algorithm for retrieving land-surface temperature from space. *IEEE Trans. Geosci. Remote Sens.,* **34,** 892–905.

——, and W. Snyder, cited 1996: MODIS land surface temperature algorithm theoretical basis document (LST ATBD). [Available online at http://modis-land.gsfc.nasa.gov/pdfs/atbd_mod11.pdf.]